PAPER

Elucidating the dominant mechanisms in burn rate increase of thermite nanolaminates incorporating nanoparticle inclusions

View the article online for updates and enhancements.

Elucidating the dominant mechanisms in burn rate increase of thermite nanolaminates incorporating nanoparticle inclusions

Baptiste Julien[1,*] , **Haiyang Wang**[2], **Emilian Tichtchenko**[1],
Sylvain Pelloquin[1], **Alain Esteve**[1], **Michael R Zachariah**[2] **and Carole Rossi**[1,*]

[1] LAAS-CNRS, University of Toulouse, 7 Avenue du colonel Roche, F-31400 Toulouse, France
[2] University of California, Riverside, CA 92521, United States of America

E-mail: bjulien@laas.fr and rossi@laas.fr

Abstract
It was experimentally found that silica and gold particles can modify the combustion properties of nanothermites but the exact role of the thermal properties of these additives on the propagating combustion front relative to other potential contributions remains unknown. Gold and silica particles of different sizes and volume loadings were added into aluminum/copper oxide thermites. Their effects on the flame front dynamics were investigated experimentally using microscopic dynamic imaging techniques and theoretically via a reaction model coupling mass and heat diffusion processes. A detailed theoretical analysis of the local temperature and thermal gradients at the vicinity of these two additives shows that highly conductive inclusions do not accelerate the combustion front while poor conductive inclusions result in the distortion of the flame front (corrugation), and therefore produce high thermal gradients (up to 10^{10} K.m^{-1}) at the inclusion/host material interface. This results in an overall slowing down of the combustion front. These theoretical findings contradict the experimental observations in which a net increase of the flame front velocity was found when Au and SiO$_2$ particles are added into the thermite. This leads to the conclusion that the faster burn rate observed experimentally cannot be fully associated with thermal effects only, but rather on chemical (catalytic) and/or mechanical mechanisms: formation of highly-stressed zones around the inclusion promoting the reactant mixing. One additional experiment in which physical SiO$_2$ particles were replaced by voids (filled with Ar during experiment) to cancel the potential mechanical effects while preserving the thermal inhomogeneity in the thermite structure confirms the hypothesis that instead of pure thermal conduction, it is the mechanical mechanisms that dominate the propagation velocity in our specific Al/CuO multilayered films.

Supplementary material for this article is available online

Keywords: energetic materials, self-propagating reaction, Al/CuO, nanolaminates, burn rate, nanoparticles, modelling

(Some figures may appear in colour only in the online journal)

1. Introduction

Considering advances in nanomaterials production and 3D printing, new energetic composites incorporating nanothermites have attracted a great deal of attention for energy generating applications [1–13]. These new materials not only have high energy density, but also release their stored chemical energy in a rapid, safe and stable manner, upon ignition. A large part of the research is still dedicated to finding ways to modulate accurately the combustion wave velocity (m.s^{-1} to hundreds of m.s^{-1}) in a

---

* Authors to whom any correspondence should be addressed.

reproducible way [14–18]. As the energy release rate is directly dependent on the equivalence ratio, size and morphology of the oxidizer and fuel, many research studies propose to manipulate the material formulation; however it requires expensive and time-consuming synthesis and characterization loops. Another empirical procedure reported in the literature consists in doping the energetic composite with additives featuring high thermal diffusivities like metals and carbon structures [19–23] to enhance the heat conduction in different areas of the energetic composite with the goal to accelerate the thermal front (flame) propagation. In [19] the authors show that inclusions of 1.5 wt% carbon nanotubes in the Mg/MnO_2/polyvinylidene fluoride (PVDF) films improved the burn rate by a factor of 4. Recently, Julien *et al.* showed that incorporation of gold nanoparticles into Al/CuO nanothermite increases the ignitability and enhances burning properties [24]. Shen *et al* [25] observed that adding Ag nanoparticles into Al/CuO nanothermite modifies the flame temperature and structure, which greatly affects the flame propagation velocity: with 4 wt% of Ag nanoparticles addition, the burn rate increases by 64% whereas for higher Ag loadings, the flame propagation slows down. Counterintuitively, we can also find in the literature that the addition of low conductive materials leads to increased burn rate. Shioya *et al* [26] added a silica-based diatomaceous earth (88 wt% SiO_2) into a propellant and measured enhanced combustion speed. Although the authors argued that the thermal insulating properties of the SiO_2 induces an increase of the temperature in the vicinity of the particles, resulting in a faster burn rate, more supporting data is needed to confirm this theory. In [27], Wang *et al* refined the analysis by incorporating 2.5 wt% of SiO_2 into Al/PVDF film: they observed an increase of the burn rate by a factor 3 compared to that of pure Al/PVDF. The authors concluded that SiO_2 promotes the formation of hot-spots that subsequently help the flame propagation; they also concluded that SiO_2 might catalyze the decomposition of PVDF.

However, the effect of additives (metals, carbons or oxides) on the combustion properties of energetic materials, either energetic composites or thermites, has been studied only macroscopically. As such, only crude mechanistic estimates are derived from the observations, leading to conflicting results. This makes it difficult to associate a faster burn rate to enhanced thermal transport properties only, which is often stated for a variety of materials that are known to exhibit radically different thermal behaviors.

This paper seeks to better understand the role of additives in reacting thermite system by observing microscopically the thermal signature of conductive *versus* insulating additives embedded in a thermite material. Specifically, the two questions are addressed in the study: What is the exact role of thermal transport properties on the observed modification in the burn rate? And what alternative mechanism(s) could be responsible for this modification?

To reach this goal, Au and SiO_2 particles were added into Al/CuO nanolaminates and their effects on the flame front behavior were investigated both theoretically and experimentally using microscopic dynamic imaging techniques. We focus our theoretical analysis on the mapping of the thermal gradients at the vicinity of additives. We subsequently
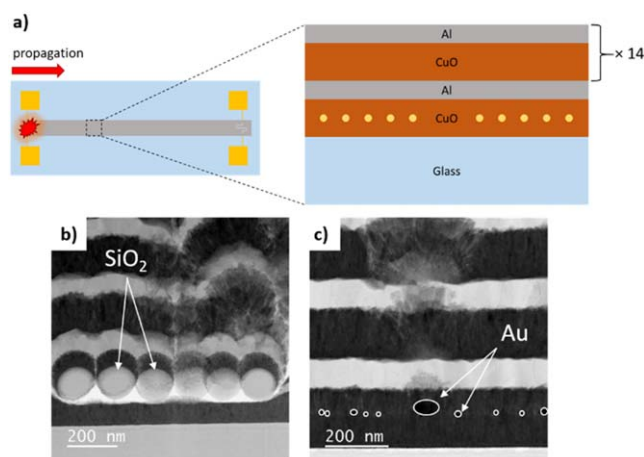
Figure 1. Front view and cross section schematic of the sample configuration (a). Electronic cross-sections of the prepared Al/CuO −SiO₂ (b), and Al/CuO−Au samples (c) where we can distinguish the embedded particles location into the first CuO layer.

analyzed the effect of the flame thermal distortion on the local velocity as well as on the self-propagating burn rate, also called global burn rate. Results demonstrate that we cannot associate the faster burn rate observed experimentally in thermites incorporating high or poor thermal conductors to thermal transport properties only. Complementary experiments on thermite nanolaminates containing voids permitted to support the conclusion that catalytic or/and mechanical effects such as the formation of highly stressed-zones surrounding the particle that can enhance locally the reactants diffusion, might play a dominant role in the observed burn rate enhancement.

2. Methods

2.1. Model-systems

A shared experimental/theoretical model-system is designed with well-known and controlled mechanical and thermal properties: It consists of 15-Al/CuO bilayers (reference), each bilayer being 225 nm thick, CuO layer being 150 nm whereas Al is of 75 nm (figure 1(a)). Into these well-defined stoichiometric nanothermite stacks (Al/CuO-reference), nanoscale SiO_2 and Au particles were incorporated into the first CuO layer of the stack, respectively named Al/CuO−SiO₂ and Al/CuO−Au. Au and SiO_2 materials were chosen as they exhibit high thermal diffusivity properties ($127 \times 10^{-6}\,m^2.s^{-1}$) and very low thermal diffusivity properties ($1.4 \times 10^{-6}\,m^2.s^{-1}$), respectively, compared to CuO ($9.9 \times 10^{-6}\,m^2.s^{-1}$). They also can be considered as chemically neutral materials compared to many others.

Al/CuO multilayers with dimensions of 25 mm (length) × 2 mm (width) were sputter-deposited onto a 32 mm (length) × 18 mm (width) × 500 μm (thick) glass slide and ignited using a resistive heated titanium wire (figure 1(a)). The Al/CuO−SiO₂ and Al/CuO−Au film electronic cross-sections show particles well organized in the first CuO layer (figures 1(b) and (c)). Silica particles
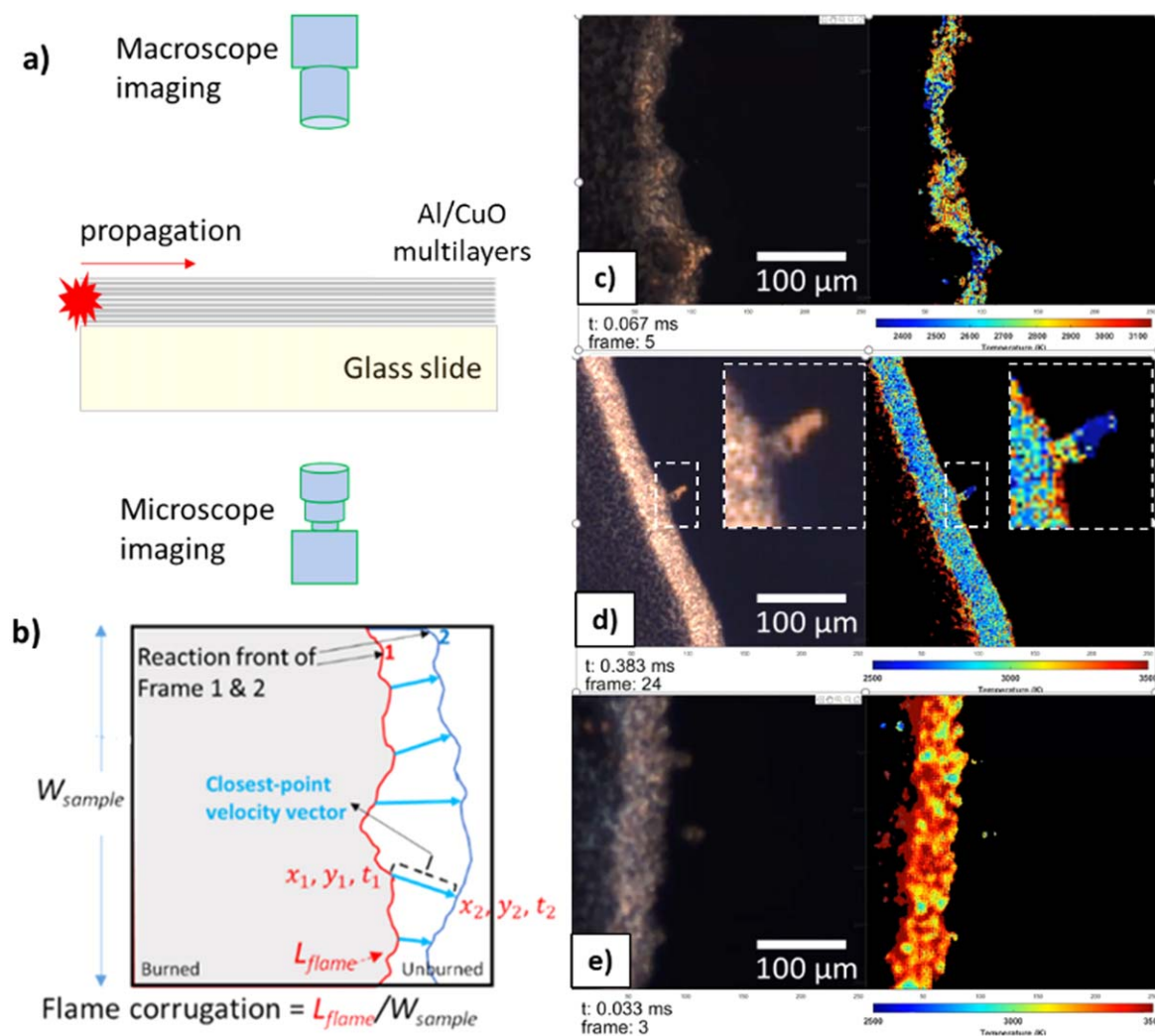
Figure 2. Experimental configuration for high-resolution pyrometry (a). Schematic showing how micro burn rate is measured (b). Snapshots from raw videos and temperature maps for the reference sample (c), Al/CuO−SiO$_2$ (d) and Al/CuO−Au (e).

(purchased from Sigma-Aldrich, France) are well-defined spheres with a diameter of 150 ± 10 nm. Gold particles are synthetized and photo-deposited following a process used in a previous work [24]. The size of deposited gold particles ranges between 5 and 30 nm with some larger aggregates reaching hundreds of nm. In all sets of tests,

2.2. Flame dynamics experimentations

We employed a previously described microscopic dynamic imaging system to record the propagation and probe the temperature profiles across the reaction zone arriving at the vicinity of the particles. The details of the dynamic imaging experiment can be found in several previous studies [28–30]. Briefly, as shown in figure 2(a), glass slides coated with Al/CuO multilayers (Al/CuO−Au and Al/CuO−SiO$_2$ samples) were mounted on a three-axis translational stage in between two camera systems with different imaging length scales. Ignition of the multilayers was achieved by applying a direct current pulse (~500 ms duration and ~1.8 A) through the embedded thin titanium line. Propagation is mirrored between

the two cameras. On the far side, a macroscopic imaging high-speed camera (Phantom V12.1) captures the front side of the combustion propagation at a resolution of 640×200 pixels (~78 μm/pixel) and a sample rate of 13 000 frames per second. The aperture was nominally f22, with a 2–6 μs exposure. The microscopic imaging system employs a high-speed camera (Phantom VEO710L) coupled to a long working distance microscope lens (Infinity Photo-Optical Model K2 DistaMax, CF-4 Objective) which provides a pixel/distance ratio of ~1.7 μm/pixel (256×256 pixels) from a working distance of ~54 mm. At this resolution, the flame front crossing a single particle and flame front could be captured and the corresponding temperature map could be obtained (figures 2(d), (e)). The microscope objective system images the back side of the sample through the transparent glass side thereby allowing the visualization of the flame front without the generated products obscuring the view. High-speed microscopy videos were recorded at a sample rate of 60 000 frames per second with an exposure of 15 μs.

The global burn rate (table 1) defined as total thermite film length/total burn time is obtained from the macroscopic

Table 1. Summary of burn rate, flame corrugation and flame temperature of each sample.

Sample	Measured global burn rate[a] (m.s^{-1})	Measured micro burn rate (m.s^{-1})	Measured corrugation	Measured flame temperature (K)
Al/CuO-ref	2.8 ± 0.1	1.94 ± 0.22	1.54	2800
Al/CuO−SiO$_2$	3.7 ± 0.1	2.77 ± 0.10	1.36	3000
Al/CuO−Au	6.1 ± 0.1	4.8 ± 0.3	1.45	3400

[a] This corresponds to the self-propagating velocity, calculated as the total thermite length/total burn time.

videos. It has to be noted that the global burn rate corresponds to the nominal burn rate that is quoted in papers. From the microscopic images as shown in figures 2(c)–(e), the flame temperature, front width, time-resolved microburn rate (closest point velocity vector), also called local velocity, and flame corrugation ($L_{\text{flame}}/W_{\text{sample}}$, figure 2(b)) are obtained.

2.3. Flame front propagation 2D model

The flame front propagation modelling was carried out using a house-built 2D non-stationary model [35] solving a coupled set of heat (equation (1)) and Fick's equations (equation (3))

$$\rho C_p \frac{\partial T}{\partial t} - \vec{\nabla}.(\lambda \vec{\nabla} T) + \vec{\nabla} \cdot \vec{F_s} = P_{Hrx} - P_{PC}, \qquad (1)$$

where ρ, C_p, λ and P_{Hrx} are respectively the local average density, the local average heat capacity, the local average heat conductivity and the power generation by the reaction, respectively. P_{Hrx} is equal to the sum of the enthalpy of formation of each species ($h_{f,i}^0$) multiplied by the rate of their production r_i, as specified in the following equation:

$$P_{Hrx} = -\sum r_i h_{f,i}^0 \qquad (2)$$

P_{PC} is the power required for the melting of the different species. Note that these are endothermic processes, which means that they do contribute negatively to the temperature. $\vec{F_s}$ is detailed later on.

The Fick's law is written as:

$$\frac{\partial C_i}{\partial t} + \vec{\nabla} \cdot (D_i \vec{\nabla} C_i) = r_i, \qquad (3)$$

where C_i and D_i are respectively the concentration and diffusion coefficient of the chemical species i. The species i are the reactants (namely Al and CuO), the products (Cu, Al$_2$O$_3$), the atomic oxygen (O) upon CuO decomposition as well as chemically inert material: Au and SiO$_2$. Taking into account that only Al and O diffusion are considered, equation (3) becomes a set of following equations:

$$\frac{\partial C_{Al}}{\partial t} + \vec{\nabla} \cdot (D_{Al} \vec{\nabla} C_{Al}) = r_{Al}, \qquad (3a)$$

$$\frac{\partial C_{CuO}}{\partial t} = r_{CuO}(\text{no CuO diffusion}), \qquad (3b)$$

$$\frac{\partial C_O}{\partial t} + \vec{\nabla} \cdot (D_O \vec{\nabla} C_O) = r_O, \qquad (3c)$$

$$\frac{\partial C_{Cu}}{\partial t} = r_{Cu}(\text{no Cu diffusion}), \qquad (3d)$$

$$\frac{\partial C_{Al2O3}}{\partial t} = r_{Al2O3}(\text{no Al}_2\text{O}_3 \text{ diffusion}), \qquad (3e)$$

$$\frac{\partial C_{Au}}{\partial t} = 0(\text{no reaction, no diffusion in Au}), \qquad (3f)$$

$$\frac{\partial C_{SiO2}}{\partial t} = 0(\text{no reaction, no diffusion in SiO}_2). \qquad (3g)$$

Note that in this work we consider that the CuO decomposes in one single step (CuO → Cu) as we focus on reaction front propagation dynamics occurring at high temperatures where the decomposition of CuO is not known to be a limiting process. The reaction rates r_i for all other chemical reactions (not detailed) follow Arrhenius laws. The prefactors and the activation energies are fitted to literature or experimental data from previous works [29–34].

The two differential equations (equations (1) and (3)) are coupled via the source term and energy fluxes, $\vec{F_s}$ which is related to species diffusion, as defined in equation (4)

$$\vec{F_s} = \sum D_i \vec{\nabla} C_i \int_{298}^T C_{p,i}(T) dT. \qquad (4)$$

Within each mesh unit-cell, the local heat capacity and heat conductivity are the average of the heat capacity and heat conductivity of each considered species weighted by their local concentration:

$$C_P(T) = \frac{\sum C_{P,i}(T) C_i}{\sum C_i} \text{ and } \lambda = \frac{\sum \lambda_i C_i}{\sum C_i}. \qquad (5)$$

The heat capacity of each species i is computed as a function of temperature using Shomate equation.

Finally, equations are solved in all the thermite system (15-Al/CuO multilayer with Au and SiO$_2$ inclusions), by using a finite volume method. The mesh size is $33 \times 6 \text{ nm}^2$ and a time step of 10^{-14} s is used. Simulation outputs give the two-dimensional temperature and species distribution at given steps of the propagation.

As initial conditions, the multilayer film is supposed to be ignited at the left end ($x = 0$), i.e. the temperature of the left boundary is set to the flame temperature, set numerically at 2843 K, corresponding to the copper vaporization point, at which we assume that the multilayer is dispersed in the gas phase. The rest of the multilayer is initially set at the ambient temperature. Since the goal of this study is not to quantify burn rates and also to save computing time, no heat loss is considered. However, diffusion coefficient values have been adjusted to get burn rate in the same order of magnitude compared to experimental values. All parameters used in the

calculations are given in supplementary information (SI), table S1 (available online at stacks.iop.org/NANO/32/215401/mmedia).

3. Results and discussions

3.1. Experimental imaging of the combustion front and local burn rate

Figure 2 presents microscopic burning snapshots of the three samples, reference, $Al/CuO-SiO_2$ and $Al/CuO-Au$, and their respective average flame temperatures. From the microscopic analysis, one can obtain the flame temperature, the micro burn rate and the flame corrugation. The global burn rate is measured as the total propagation distance over the total burn time. All the experimental values are summarized in table 1. Quite clearly, we see that, when compared to the Al/CuO-ref, addition of SiO_2 and Au NPs speeds up the reaction front locally as well as the flame temperature. For Al/CuO-ref, the local burn rate is 1.94 ± 0.22 m.s^{-1} with an average flame temperature of 2800 K. $Al/CuO-Au$ sample features the highest value: 4.8 ± 0.3 m.s^{-1} and 3400 K. For $Al/CuO-SiO_2$, micro burn rate is measured at 2.77 ± 0.10 m.s^{-1} and temperature stabilizes at 3000 K.

It is noticeable that the addition of Au and SiO_2 particles does not modify much the flame front spatial spreading over time. We measured the flame corrugation as the ratio of the total geometrical length of the flame to width of the sample in the direction perpendicular to propagation. It turns out that the flame corrugation is even slightly lowered with additives (see error bars), which might be due to the increase of the global burn rate and temperature trimming the front in a stoichiometric reference system that commonly shows low corrugation (see [28]).

In $Al/CuO-SiO_2$ case, the local burning snapshot (figure 2(d)) shows the flame approaching an object that we assimilate to a SiO_2 particle or aggregate. By zooming in it, we can see that the inclusion is cold, as indicated by the color mapping, regarding the combustion front. It is coherent as silicon dioxide has a low thermal diffusivity, and thus inhibits heat conduction. Unfortunately, in the $Al/CuO-Au$ sample, the detailed imaging sequence at the crossing over of the flame front and Au inclusion was more difficult to capture due to the extensively high burn rate.

To capture and further understand the experimental observations, we successively modelled the flame front propagation across one single nanoparticle and several nanoparticles randomly placed. The dimensions and thermal properties of these inclusions are set comparable to those used experimentally.

3.2. Analysis of thermal gradient and flame velocity around a single nanoparticle

In this part, one 130 nm $\times$ 44 nm nanoparticle of SiO_2 or Au (also called inclusion or additive) is embedded into the first CuO layer of the stoichiometric 15-Al/CuO multilayers.

From the two-dimensional time temperature distribution and around the inclusion, we mapped the normed temperature gradient, defined as $\|\vec{\nabla}T\| = \sqrt{(\Delta T/\Delta x)^2 + (\Delta T/\Delta y)^2}$ at three different moments of propagation: the flame front approaches the inclusion (t_1), crosses it (t_2), and after passing through it (t_3). This enables us to better picture the flame morphology and the thermal impact of the inclusion. In figure 3, the gradient field is represented by a color map: dark blue corresponds to a uniform temperature distribution ($\vec{\nabla}T = 0$) whereas bright yellow indicates extreme gradient areas reaching 10^{10} K.m^{-1}.

The flame corresponds to the reaction zone where the thermal gradient between unburnt reactants (forward) and products (backward) is high (see figure 3(c)). A zoom at the inclusion location (red box) allows visualizing the gradient distribution around the particle.

At t_1, i.e. before reaching the inclusion, the flame front is straight, with a thickness of 1 μm, for both systems. The flame front is much thinner than the experiment measured by high-resolution pyrometry in figure 1 ($\sim$50 μm). This is simply explained by the fact that no thermal loss was implemented within the model, thus all the reacted materials remain at the fixed reaction temperature.

At t_2, i.e. when the flame front reaches the inclusion, we notice an important difference between these two modelled systems. For $Al/CuO-SiO_2$, temperature gradients up to 10^{10} K.m^{-1} are developing at the cross-sectional surface area of silica particle. The low thermal diffusivity of SiO_2 (1.4×10^{-6} m^2.s^{-1}) inhibits the heat conduction around the particle leading to the creation of hot-points, characterized by high thermal gradient zones. In contrast, $Al/CuO-Au$ does not exhibit a sharp thermal gradient, which is consistent with the higher thermal diffusivity of Au. The relative change in the temperature gradient (in % compared to the minimum value) along the y-axis, starting into the inclusion, is plotted in figure 4 for both systems. Interestingly, the SiO_2 particle thermally affects the surrounding material over a larger range ($\sim$0.7 μm) than the Au particle does. The gradient decreases by $\sim$24% along the y-axis whereas the gradient only changes by $\sim$1.5% for Au case. Moreover, a slight bump is observed for the $Al/CuO-Au$ system, and an inflection for $Al/CuO-SiO_2$, around 0.24 μm, corresponding to the area where the local reaction between CuO and Al initiates (the initial location of the CuO/Al interface). A color map, showing the instantaneous distribution of alumina (at t_2), supports this statement (see SI, figure S3).

At t_3, after the flame front has passed the inclusion, the Au particle has still no effect on the thermal front, whereas high thermal gradients still persist at the SiO_2 interface. This is again explained by the very low thermal diffusivity of silica, which induces a high thermal inertia. Hence, the SiO_2 particle and its vicinity take more time to thermalize, compared to gold.

In addition to thermal gradients, a feature of interest in these types of simulations is the instantaneous reaction front velocity, which is unreacheable experimentally at our sampling rates. In our model, local or instantaneous front
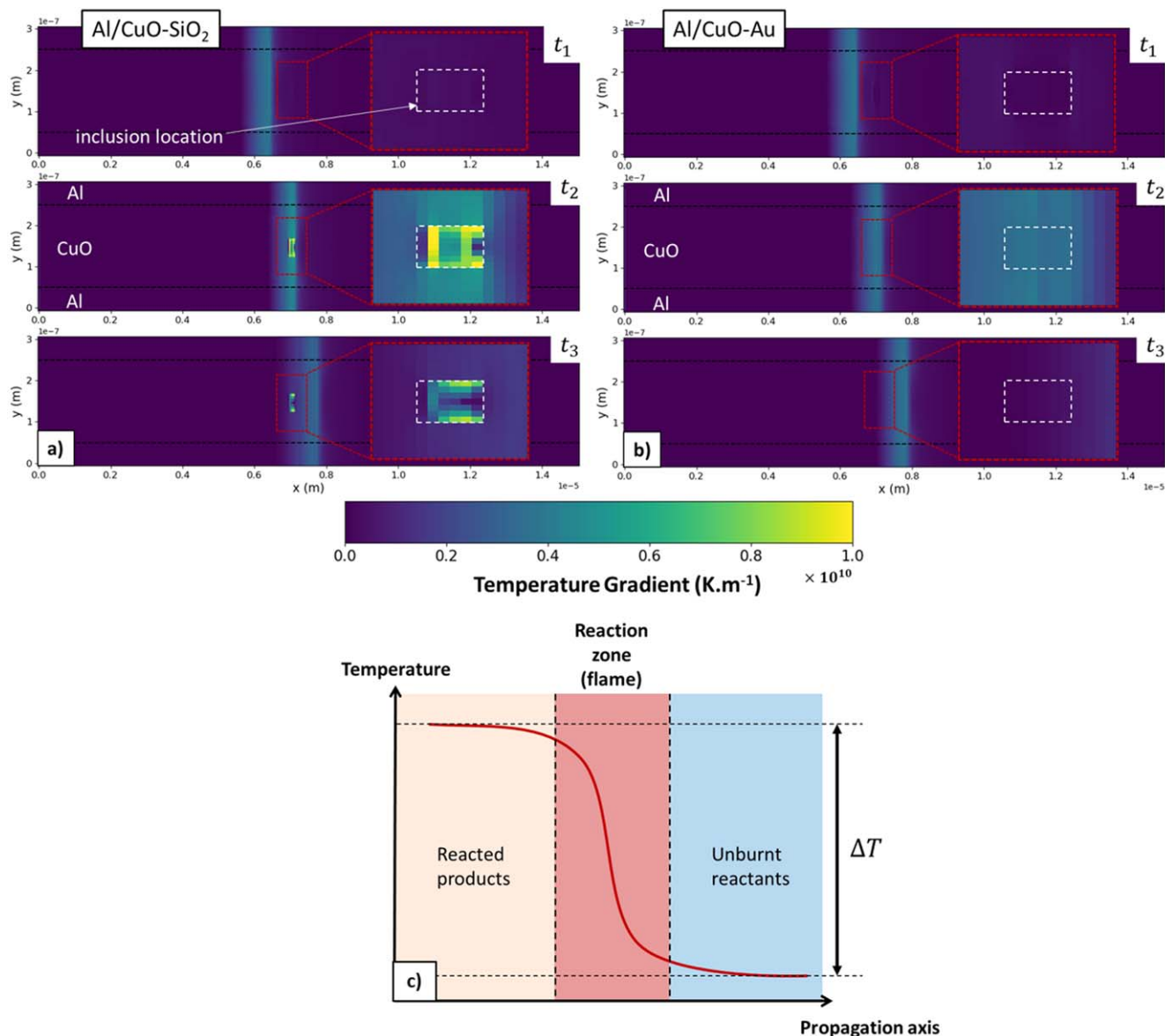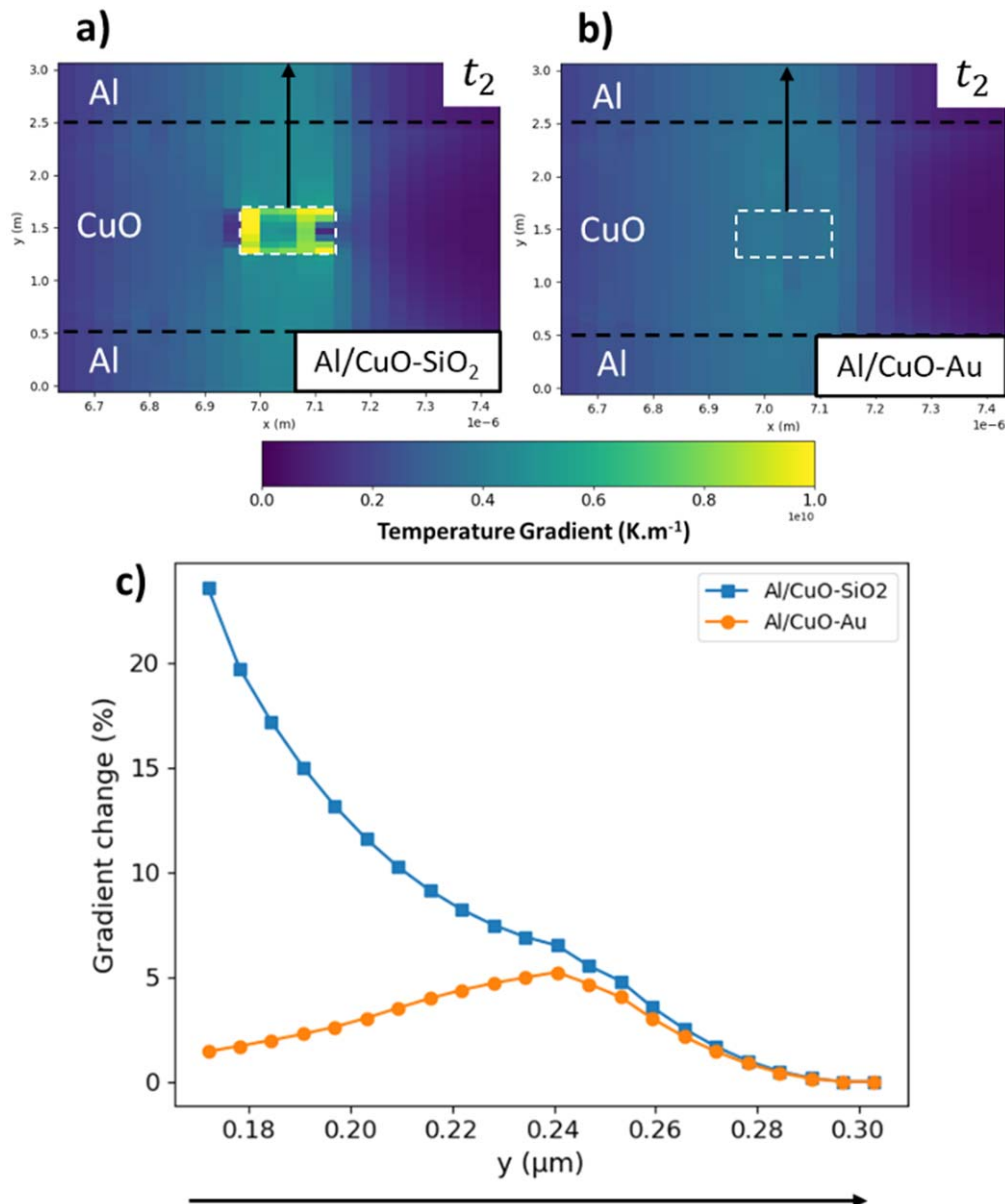
Figure 3. 2D maps of the temperature gradient taken at three different times for Al/CuO−SiO$_2$ (a) and Al/CuO−Au (b) systems. The red boxes correspond to zooms around the inclusion, itself indicated by the white dashed square. Black horizontal lines indicate the interfaces between Al and CuO layers. The flame is approaching the inclusion ($t_1 = 1.40$ μs), is crossing the particle ($t_2 = 1.56$ μs) and has passed the particle ($t_3 = 1.72$ μs). (c) Typical temperature profile for a self-propagating reaction in which the flame corresponds to the reaction zone (in red).

velocities v_y are determined at time t, from the time-temperature histories of two neighboring cells along x-axis, for each y position. Then, for each time t, an y-averaged front velocity is calculated, also called mean front velocity, v. The velocities v_y inside the inclusion are not considered for the calculation of v as it has no physical meaning. Finally, in figure 5, we plot the mean front velocity along the propagation axis, x, regarding the global burn rate in each cases.

In the reference system, without inclusion (green dashed curve), the flame front propagates with a constant mean front velocity of 4.45 m.s^{-1}. For both Al/CuO−SiO$_2$ and Al/CuO−Au, a strong thermal perturbation is observed when the flame crosses the inclusion. Specifically, we can distinguish 3 phases on the velocity diagram of figure 5: (1) Just before reaching the inclusion, the front accelerates up to 5.4 m.s^{-1}

for Al/CuO−SiO$_2$ (blue curve), whereas Au particle (orange curve) induces a slow-down. (2) then, the presence of the inclusion provokes a sharp velocity drop to 3.4 m.s^{-1} for SiO$_2$ case (−24% compared to global velocity). Gold induces the opposite effect as we observe a local acceleration, up to 5.3 m.s^{-1} (+20%). (3) Finally, after passing the inclusion, the simulations show that, for both cases, the combustion front regains its steady state after a pseudo-oscillating regime due to thermal instability. The overall flame perturbation extends over approximately 2.2 μm and 1.8 μm for SiO$_2$ and Au case respectively. Considering the length of the embedded nanoparticle (0.13 μm), the perturbation range corresponds respectively to 17 times and 14 times the particle length.

Although the particles embedded into the CuO layer affect the front velocity locally, these simulations show that

Figure 4. Relative change (%) of the temperature gradient at time t_2 (1.56 μs) along the *y*-axis and following the vertical line above the particle (black arrows drawn on the gradient maps), for Al/CuO−SiO$_2$ and Al/CuO−Au systems.

the global burn rate rapidly return back to its base case within a microsecond.

3.3. Influence of the volume loading on the flame velocity

In order to discuss the interplay of multiple inclusions, as well as to gain more insight into the burn rate modification observed experimentally, we vary the volume percentage (vol%) of the additives into the 15-Al/CuO multilayered thermite, and we look now at the self-propagating combustion velocity. The first case consists in adding multiple nano-inclusions while keeping the size of the single inclusion at 130×44 nm^2. We performed four simulations including 1, 7, 14 and 20 inclusions (respectively pictured in figures 6(a)–(d)). The nano-inclusions are always randomly placed with an inter-particle distance spanning from 100 nm to 2.5 μm.

Figure 6 shows the change in the global burn rate (in %, compared to the reference at 4.45 m.s^{-1}) as a function of the volume loading, for both Al/CuO−SiO$_2$ and Al/CuO−Au systems. The results show that the velocity changes linearly with increasing volume loading of embedded inclusions, but with opposite trends. Specifically, the higher thermal conductor results in a small increase in velocity (up to 4%), while the low thermal conductor, silica has a more dramatic effect decreasing burn rate by as much as 17%.

Unfortunately, this conflicts with the experimental observation (section 2.1) which shows higher burn rate for both types of inclusions. Hence, we may conclude that the impact of the thermal properties of nanoscale additives on the propagating combustion front in thermite materials is not determinant.
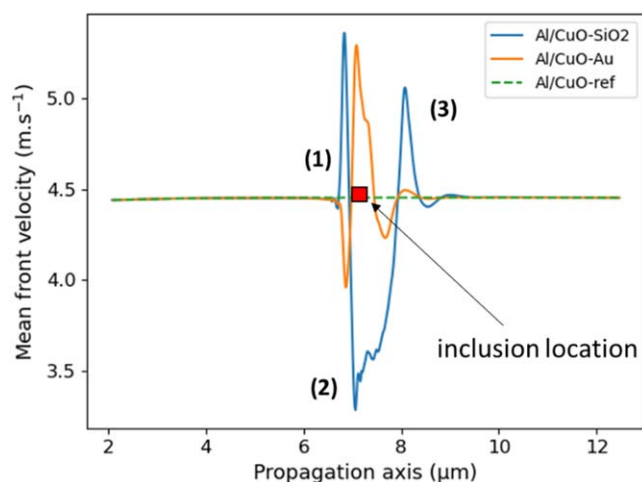
Figure 5. Mean front velocities (*v*) along the propagation axis, in Al/CuO−SiO₂ (blue curve), Al/CuO−Au (orange curve) and Al/CuO-ref (green dashed curve). The red square represents the location of the nano-inclusion.

Next, we consider the effect of the size of the embedded particle on the thermal profile of the flame and its velocity. One or several Au and SiO₂ micro-particles ($2 \times 1 \ \mu m^2$) were embedded into a full stoichiometric thermite stack (15 Al/CuO bilayers, see SI, figure S4). In term of volume loading, it corresponds to 1.5%.

To better picture the effect of the inclusion size, the 2D temperature maps are plotted at five different times of propagation picturing the flame front crossing the inclusion (figure 7). In both cases, the deformation of the flame front before it reaches the inclusion is very similar to the experimental observation as discussed and seen in figure 3(d), with a local spreading of the heat towards the inclusions, upfront to the propagating flame. After crossing the inclusion, at $t = 3.5 \ \mu s$, the SiO₂ micro-particle corrugates the reaction front by absorbing heat, thus inhibiting heat diffusion. On the other hand, the thermal footprint of the SiO₂ inclusion remains significant over the whole crossing over process. In addition, the following snapshots show that the reaction front extinguishes ($t = 3.9 \ \mu s$), before re-igniting ($t = 4.1 \ \mu s$). This thermal behavior has a direct impact on the flame velocity. In the figure 7(c), we observe that for SiO₂ case, the mean front velocity drops below $2 \ m.s^{-1}$. This phase corresponds to the flame extinction we observe on the temperature map. Then, the combustion front accelerates up to $6.7 \ m.s^{-1}$ (re-ignition phase) and finally recovers a steady state combustion. Interestingly, the effect of the gold micro-particle on the flame front is very different. The flame front deformation is weak: it becomes slightly convex, pointing to the gold inclusion, as gold transfers the heat upstream of the flame better. Regarding the overall propagation, the gold micro-inclusion does not affect the global burn rate, contrary to the SiO₂ particle which negatively impacts the propagation, especially because of the 'quasi-quenching' of the reaction. Specifically, SiO₂ micro-particle lowers the global burn rate by 9%, which fits surprisingly with the linear relation in figure 6, as the volume

loading here is 1.5%. This supports the fact that the size of the inclusion is not the relevant parameter but rather the volume loading, regarding global burn rate changes

3.4. Discussion

Simulations confirmed that the thermal perturbations in the combustion front due to the presence of additives (being Au or SiO₂) locally impact the flame dynamics which is characterized by the local velocity. When the additive loading increases, the thermal perturbations can also modify the self-propagating burn rate positively (Au) or negatively (SiO₂). We theoretically showed that the size of the particle, especially for SiO₂, is an important factor: A nano-inclusion (a decade smaller than the thermite film thickness) affects the flame behavior locally over a distance of ∼17 times the particle size, whereas, a micro-particle (in the size range of the thermite film thickness) has a much more brutal and local effect over a distance of ∼2 times the particle size, which can provoke the flame quenching.

Surprisingly, simulations give a much smaller burn rate impact than that observed with *in operando* experiments (table 2), leading to the conclusion that the thermal mechanisms, such as heat conduction, is not the only nor the dominant process in the burn rate increase observed in thermites doped with metallic and oxide particles. Instead, we suggest that chemical and/or thermo-mechanical mechanisms might contribute.

3.4.1. Thermo-mechanical. Upon the propagating hot thermal wave, high thermal stresses might appear at the additive interface. As thermal stresses are mostly influenced by temperature gradient ($\epsilon_T = \alpha \ \Delta T$, where α is the thermal expansion coefficient), such phenomena might happen in the case of non-conductive additive such as SiO₂, as we showed high gradient zones developing at their vicinity (figures 3, 4). For the Au case, as no such gradient is observed, the strong difference of thermal expansion coefficients between CuO ($\alpha_{CuO} = 0.3 \times 10^{-7} \ K^{-1}$) and Au ($\alpha_{Au} = 142 \times 10^{-7} \ K^{-1}$) might provoke thermal stresses at their interfaces. These stresses locally promote the reactants mixing, either through energetic diffusion pathway modification, or by crack propagation, both increasing overall reaction rate. This phenomenon is accompanied by a local increase of produced heat and temperature that can correspond to what is commonly termed 'hot-spots'.

3.4.2. Chemical. Considering metal or oxide particles especially used in propellant mixture, we cannot exclude their possible catalytic effect on the reaction rate. Gold can provide electrons to catalyze oxidizer decomposition as well as to lower the activation energy of oxygen migration pathways. On the other hand, SiO₂ might engage reactions by locally providing oxygen atoms to the system.

However, considering the present work and recent findings in [24], we believe that the mechanical effect appears to be the dominant cause. Indeed, looking at the figure 1, the silica and to a lesser extent the Au nanoparticles
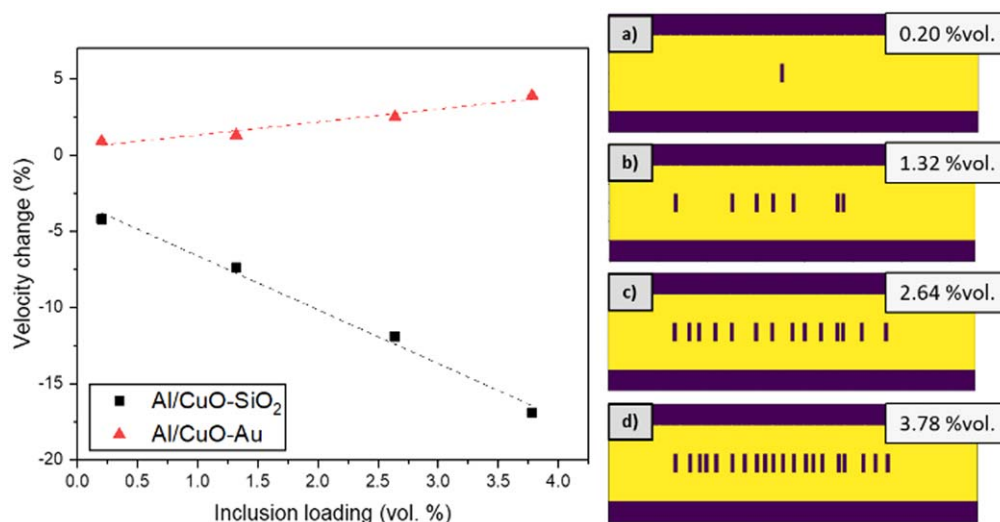
Figure 6. Relative change of the self-propagating velocity (global burn rate) for different loadings (in vol%), for Al/CuO−SiO$_2$ and Al/CuO −Au systems. Dash lines correspond to a linear fit. The graphics on the right side are schematics of simulated cases for the different loadings (1, 7, 14 and 20 nano-objects) where the inclusions are indicated by small dark rectangles.

are seeding nodular defects with conical shapes, which mechanically weakens the multilayer. Thus, the Al+CuO reaction can be readily triggered in these local zones. In [24, 31], such nodular defects were shown to provide reaction pathways along the conical shape, in axis transverse from the thermite layering. These were shown to affect much initiation delays and self-propagation velocities and a correlation to mechanical stress loading was evidenced.

With the purpose to confirm the hypothesis that incorporating SiO$_2$ particles accelerate the self-propagation velocity (experimental observations) by a mechanical rather than a thermal effect, we designed an additional experiment. We produced stoichiometric 15-Al/CuO multilayers (same as those of section 2.1) with microscale round holes (diam. 100 μm). Experiments were performed under Ar neutral atmosphere, so that the voids are filled with Ar. At room temperature, Ar has a thermal diffusivity of 20×10^{-6} m^2.s^{-1}; ten times of silica. Such holes offer the advantage to be chemically inert mechanically neutral, regarding the multilayered structure. Voids are 250 μm apart in y-axis (perpendicular to propagation) and 1 mm apart in x-axis (propagation direction) ensuring no thermal interaction between them. A distance of 5 mm on each side of the thermite line is free of voids (reference area), in order to compare the flame velocity inside and outside the void area. Details on sample designs can be found in SI, figure S5. Figure 8 gives macroscopic images of the global propagation and local front snapshots focused around one hole. From the macroscopic view, the global velocity is measured at 4.5 m.s^{-1} in the reference area (no void), and there is no noticeable acceleration in the voids area. Overall, we observe a general trend in the crossing of the void that is similar to the presented simulations when considering SiO$_2$ inclusions. The flame front is slightly corrugated when passing the voids, indicating a lowering of local burn rate at the close vicinity of

the void. Interestingly, after passing the void, the flame front is clearly deformed in a similar 'V' shape as observed in the simulation (figure 8(a)), but seems to recovery rapidly. In addition, we can notice an increase in the temperature inside the void before the crossing of the flame, probing the flame plume, hot particles ejected upfront and hot gas convection. Assuming that the use of voids cancels the mechanical contribution, and can be compared with the case of simulations of SiO$_2$ inclusions purely in term of heat transport, leads to the conclusion that the deviation to higher velocity experimentally observed should match with a dominant mechanical origin taking place at around the particles locations.

4. Conclusion

In order to rationalize the numerous studies published over the last few decades affirming that additives with high thermal diffusivity and sometimes low thermal diffusivity are able to increase the burn rate by enhancing heat conduction to different areas of the energetic material, we examined microscopically and both theoretically and experimentally, the thermal effect of gold and silica inclusions on the propagating combustion front in Al/CuO nanothermite. The simulations used a 2D non-stationary reaction model taking into consideration both oxygen and Al diffusion and allowing the 2D temperature and species mapping by solving the differential equations for heat and mass transport in x (propagation axis) and y axis (perpendicular to the propagation axis). The experiments were based on both macro and microscale high speed imaging/pyrometry. While the experimental observations of thermite containing such inclusions show drastic enhancement of the burn rate, the simulation results indicate that, under low loadings (<3.5% vol), (i) poor conductive
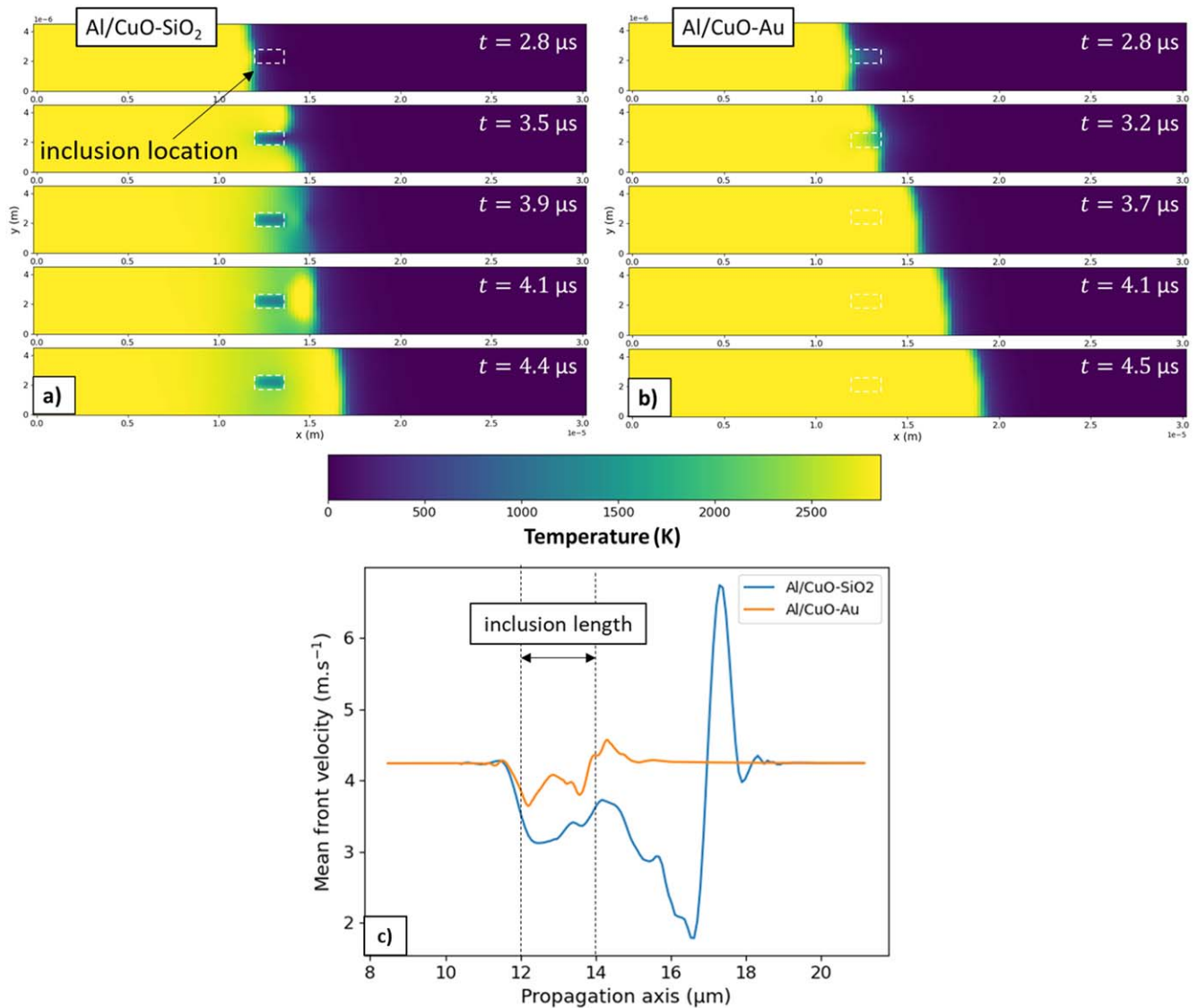
Figure 7. 2D maps of the temperature for Al/CuO−SiO$_2$ (a) and Al/CuO−Au (b) systems including a microsized inclusion (2 μm × 1 μm) inside, taken at several times. The inclusion is highlighted by the dash box. (c) Plots of the mean front velocities along the propagation axis, for both systems, Al/CuO−Au and Al/CuO−SiO$_2$. The arrow represents the particle length.

Table 2. Main results to be confronted for the discussion.

Sample	Velocity change relative to reference (%)	
	Experiments	Simulation
Al/CuO−SiO$_2$	+32	−20
Al/CuO−Au	+117	+4

inclusions should slow down the flame velocity up to 17% maximum, (ii) highly conductive materials should not change much the flame velocity (+4% at the maximum).

This leads to the conclusion that the faster burn rate observed experimentally cannot be fully associated with thermal effects only. Instead, we propose that other chemically and/or mechanically based processes must play a

dominant role. Further experiments performed with void additives as mechanically free model-systems allows us to confirm the dominant role of thermo-mechanical mechanisms at the source of burn rate enhancement in thermite containing either poor or high thermal conductor inclusions. Specifically, we propose that the propagating hot thermal wave engenders and/or magnifies existing highly-stressed zones at the interface of the particles and matrix. Moreover, extreme thermal gradients or differences in mechanical properties between the oxidizer matrix and the embedded particle might create additional local thermal stresses. All of this leads to a local enhancement of reactant mixing, which in turn enhances the global rate. The local reaction generating additional heat might be the mechanistic source of what is commonly called 'hot-spots'. This paper proposes a new way of thinking the effect of additives in burn rate of
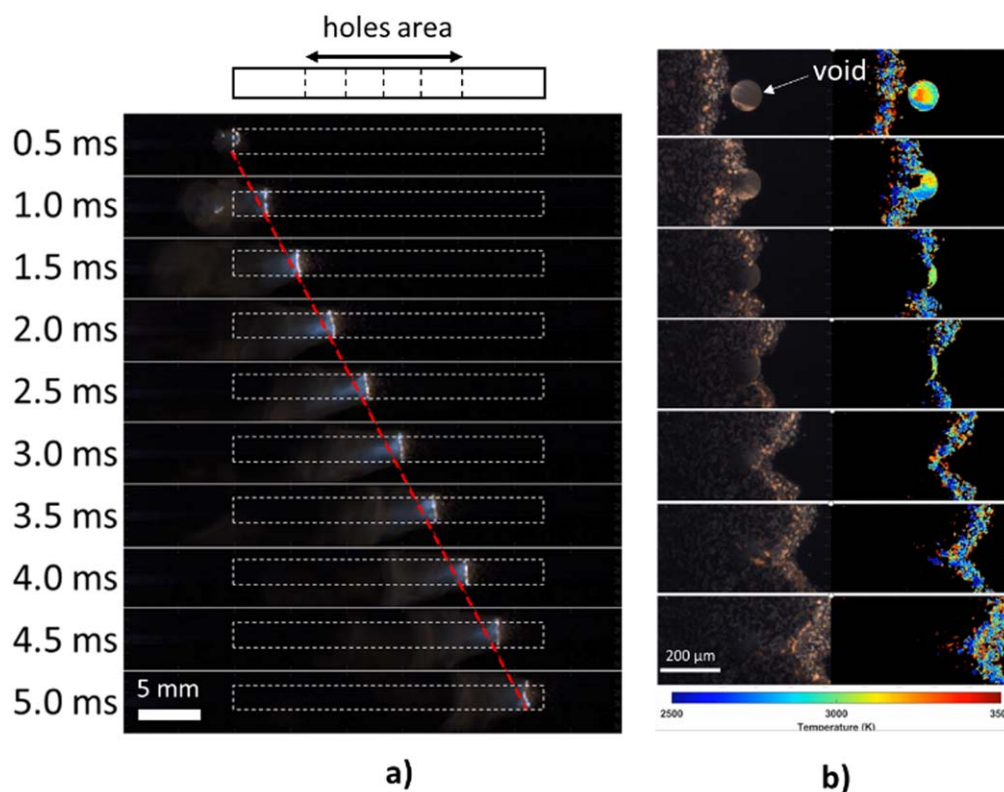
Figure 8. Macroscopic images of self-propagating reaction for Al/CuO-voids sample (a) and local burn snapshots focused around one void (b). The dashed line indicates the burn rate is constant.

energetic materials and opens new research directions to provide further fundamental supporting evidences and to suggest innovating materials.

Data availability statement

All data that support the findings of this study are included within the article (and any supplementary files).

ORCID iDs

Baptiste Julien ⦾ https://orcid.org/0000-0002-4297-3455

References

[1] Rossi C 2017 Innovating in energetic materials from the bottom *Propellants Explos. Pyrotech.* **42** 235–6
[2] Nicollet A *et al* 2017 Investigation of Al/CuO multilayered thermite ignition *J. Appl. Phys.* **121** 034503
[3] McCollum J *et al* 2015 Catalyzing aluminum particle reactivity with a fluorine oligomer surface coating for energy generating applications *J. Fluorine Chem.* C 265–71
[4] Staley C S *et al* 2011 Silicon-based bridge wire micro-chip initiators for bismuth oxide–aluminum nanothermite *J. Micromech. Microeng.* **21** 115015
[5] Glavier L *et al* 2015 Nanoenergetics as pressure generator for nontoxic impact primers: comparison of Al/Bi$_2$O$_3$, Al/CuO, Al/MoO$_3$ nanothermites and Al/PTFE *Combust. Flame* **162** 1813–20
[6] Dai J *et al* 2020 From nanoparticles to on-chip 3D nanothermite: electrospray deposition of reactive Al/ CuO@NC onto semiconductor bridge and its application for rapid ignition *Nanotechnology* **31** 195712
[7] Apperson S J *et al* 2009 Characterization of nanothermite material for solid-fuel microthruster applications *J. Propul. Power* **25** 1086–91
[8] Korampally M *et al* 2012 Transient pressure mediated intranuclear delivery of FITC-Dextran into chicken cardiomyocytes by MEMS-based nanothermite reaction actuator *Sensors and Actuators B: Chemical* **171–172** 1292–6
[9] Nicollet A *et al* 2018 Fast circuit breaker based on integration of Al/CuO nanothermites *Sensors Actuators* A **273** 249–55
[10] Wu T *et al* 2019 Silver ferrite: a superior oxidizer for thermite-driven biocidal nanoenergetic materials *RSC Adv.* **9** 1831–40
[11] Bhattacharya S *et al* 2006 A novel on-chip diagnostic method to measure burn rates of energetic materials *J. Energetic Mater.* **24** 1–15
[12] Pezous H *et al* 2010 Fabrication, assembly and tests of a MEMS-based safe, arm and fire device *J. Phys. Chem. Solids* **71** 75–9
[13] Rossi C *et al* 2006 Solid propellant microthrusters on silicon: design, modeling, fabrication, and testing *J. Microelectromech. Syst.* **15** 11

[14] Jacob R J *et al* 2019 Pre-stressing aluminum nanoparticles as a strategy to enhance reactivity of nanothermite composites *Combust. Flame* **205** 33–40

[15] Mao Y *et al* 2019 3D printing of micro-architected Al/CuO-based nanothermite for enhanced combustion performance *Advanced Engineering Materials* **21** 1900825

[16] Woodruff C *et al* 2020 Thermite reactivity with ball milled aluminum-zirconium fuel particles *Combust. Flame* **211** 195–201

[17] Bezmelnitsyn A *et al* 2010 Modified nanoenergetic composites with tunable combustion characteristics for propellant applications *Propellants Explos. Pyrotech.* **35** 384–94

[18] Thiruvengadathan R *et al* 2012 Combustion characteristics of silicon-based nanoenergetic formulations with reduced electrostatic discharge sensitivity *Propellants Explos. Pyrotech.* **37** 359–72

[19] Smith D K *et al* 2017 Thermal and combustion properties of energetic thin films with carbon nanotubes *J. Thermophys. Heat Transfer* **31** 646–50

[20] Sui H *et al* 2018 Interaction between single-walled carbon nanotubes and reactive nanoparticle constituents in multilayered Al/NiO nanocomposite *ACS Appl. Energy Mater.* **1** 5245–56

[21] Bach A *et al* 2015 Modulation of the reactivity of a WO3/Al energetic material with graphitized carbon black as additive *J. Energetic Mater.* **33** 260–76

[22] Rossi C 2019 Engineering of Al/CuO reactive multilayer thin films for tunable initiation and actuation *Propellants Explos. Pyrotech.* **44** 94–108

[23] Abdallah I *et al* 2018 structure and chemical characterization at the atomic level of reactions in Al/CuO multilayers *ACS Appl. Energy Mater.* **1** 1762–70

[24] Julien B *et al* 2020 integration of gold nanoparticles to modulate the ignitability of nanothermite films *ACS Appl. Nano Mater.* **3** 2562–72

[25] Shen J *et al* 2014 Effects of nano-Ag on the combustion process of Al−CuO metastable intermolecular composite *Appl. Therm. Eng.* **62** 732–7

[26] Shioya S *et al* 2014 Burning characteristics of ammonium perchlorate-based composite propellant supplemented with diatomaceous earth *Combust. Flame* **161** 620–30

[27] Wang H *et al* 2018 Mesoporous silica spheres incorporated aluminum/poly (vinylidene fluoride) for enhanced burning propellants *Adv. Eng. Mater.* **20** 1700547

[28] Wang H *et al* 2020 Probing the reaction zone of nanolaminates at ∼μs time and ∼μm spatial resolution *J. Phys. Chem.* C **124** 13679–87

[29] Wang H *et al* 2019 In-operando high-speed microscopy and thermometry of reaction propagation and sintering in a nanocomposite *Nat. Commun.* **10** 3032

[30] Kline D J *et al* 2020 Experimental observation of the heat transfer mechanisms that drive propagation in additively manufactured energetic materials *Combust. Flame* **215** 417–24

[31] Zapata J *et al* 2019 Self-propagating combustion of sputter-deposited Al/CuO nanolaminates *Combust. Flame* **205** 389–96

[32] Lanthony C 2012 Formation of Al/CuO bilayer films: basic mechanisms through density functional theory calculations *Thin Solid Films* **520** 4

[33] Baijot V *et al* 2015 Modeling the pressure generation in aluminumbased thermites *Propellants Explos. Pyrotech.* **40** 11

[34] Lanthony C *et al* 2014 Elementary surface chemistry during CuO/Al nanolaminate-thermite synthesis: copper and oxygen deposition on aluminum (111) surfaces *ACS Appl. Mater. Interfaces* **6** 15086–97

[35] Tichtchenko Emelian, Estève Alain and Rossi Carole 2021 Modeling the self-propagation reaction in heterogeneous and dense media: Application to Al/CuO thermite *Combustion and Flame* **228** 173–83